







Article

Organic–Inorganic Manganese (II) Halide Hybrid Combining the Two Isomers Cis/Trans of $[\text{MnCl}_4(\text{H}_2\text{O})_2]$: Crystal Structure, Physical Properties, Pharmacokinetics and Biological Evaluation

Mansoura Bourwina ¹, Sandra Walha ¹, Najeh Krayem ², Riadh Badraoui ^{3,4,*} , Faten Brahmi ⁵,
Wejdan M. Alshammari ³ , Mejdi Snoussi ³ , Mark M. Turnbull ⁶ , Thierry Roisnel ⁷  and Houcine Naïli ¹ 

- ¹ Laboratoire Physico-Chimie de l'Etat Solide, Département de Chimie, Faculté des Sciences de Sfax, Université de Sfax, B.P. 1171, Sfax 3000, Tunisia
- ² Laboratory of Biochemistry and Engineering of Lipases, National School of Engineering of Sfax (ENIS), University of Sfax, Sfax 3000, Tunisia
- ³ Laboratory of General Biology, Department of Biology, University of Ha'il, Ha'il 81451, Saudi Arabia
- ⁴ Section of Histology-Cytology, Faculty of Medicine of Tunis, University of Tunis El Manar, La Rabta-Tunis 1007, Tunisia
- ⁵ Laboratory of Organic Chemistry, Department of Chemistry, University of Ha'il, Ha'il 81451, Saudi Arabia
- ⁶ Carlson School of Chemistry and Biochemistry, Clark University, Worcester, MA 01610, USA
- ⁷ Institut des Sciences Chimiques de Rennes UMR 6226 CNRS-Université Rennes1 Campus de Beaulieu France, F-35000 Rennes, France
- * Correspondence: badraouir@yahoo.fr

Abstract: A manganese (II) complex templated by hexahydro-1,4-diazepinedium as a counter ion was grown by slow evaporation from an aqueous solution at room temperature. The X-ray diffraction analysis revealed that the compound $(\text{C}_5\text{H}_{14}\text{N}_2)[\text{MnCl}_4(\text{H}_2\text{O})_2]$ crystallizes in the centrosymmetric space group P2/c of the monoclinic system. The crystal structure of the Mn(II) complex is characterized by an alternation of 0-dimensional organic and inorganic stacks linked together by N/O-H . . . Cl and N-H . . . O hydrogen bonds, which lead to a three-dimensional supramolecular architecture. In this structure, the inorganic layer is built up by independent anionic moieties combining the two isomers cis/trans of $[\text{MnCl}_4(\text{H}_2\text{O})_2]^{2-}$. The thermal decomposition was studied by TGA-DTA techniques. The optical band gap and Urbach energy were obtained by Tauc's equation. The direct and indirect band gap values are found to be 4.58 and 4.44 eV, respectively. Weak antiferromagnetic interactions are present in the molecule under study, according to magnetic measurements. An agar well diffusion technique was used to assess the synthetic compound's biological activity, and the results showed that it has potent antibacterial (Gram-positive and Gram-negative) properties. Interestingly, the synthesized compound also displayed antilipase activity. These biological activities have been confirmed by the bioavailability and pharmacokinetic analyses.

Keywords: manganese (II) complex; thermal analysis; infrared spectroscopy; optical band gap; magnetic properties; pharmacokinetics; biological activity



Citation: Bourwina, M.; Walha, S.; Krayem, N.; Badraoui, R.; Brahmi, F.; Alshammari, W.M.; Snoussi, M.; Turnbull, M.M.; Roisnel, T.; Naïli, H. Organic–Inorganic Manganese (II) Halide Hybrid Combining the Two Isomers Cis/Trans of $[\text{MnCl}_4(\text{H}_2\text{O})_2]$: Crystal Structure, Physical Properties, Pharmacokinetics and Biological Evaluation. *Inorganics* **2023**, *11*, 76. <https://doi.org/10.3390/inorganics11020076>

Academic Editor: Yue Wang

Received: 6 January 2023

Revised: 29 January 2023

Accepted: 31 January 2023

Published: 4 February 2023



Copyright: © 2023 by the authors. Licensee MDPI, Basel, Switzerland. This article is an open access article distributed under the terms and conditions of the Creative Commons Attribution (CC BY) license (<https://creativecommons.org/licenses/by/4.0/>).

1. Introduction

Organic–inorganic hybrid materials have attracted a special attention during the recent decades. In doing so, they progressively offered the possibility to reach considerable development across different sectors [1–3]. These components exhibit fascinating properties in areas such as luminescence, optics, magnetism, and biological activity [4,5]. Previous works showed that the crystal engineering of supramolecular architectures depends on different criteria including the type of the metal (alkali earth metal, transition metal, alkali metal, other), the geometry of coordination around the metal ion, the characteristics of the organic molecule (aliphatic, aromatic, chain length, etc.), the halide ion (Br, Cl, I), and the bonding (ionic, covalent, coordination bonds, and van der Waals (vdW) forces) [6].

Furthermore, hydrogen bonding reveals the structure of coordination complexes, which link low-dimensional entities into high-dimensional supramolecular networks [7,8]. Mn^{2+} -included materials have been recently proposed as excellent component classes, which help in the creation of new materials with excellent physico-chemical properties [9,10]. During the recent three years, manganese (II) has provided interest in the field of solar cell and luminescent materials due to its tunable emission, high luminescence efficiency, and light absorption in the UV–Vis region [11–13]. Most studies about these compounds have shown that the luminescence of manganese (II) halide hybrids can be ascribed to the ${}^4T_1 \rightarrow {}^6A_1$ electronic transition of Mn^{2+} , which can be easily affected by the coordination environment of Mn(II) center [14,15]. In general, octahedrally and tetrahedrally coordinated manganese (II) complexes emit red-orange or green light, respectively [16]. In addition, for Mn^{2+} compounds, two distinct groups of absorption bands are obviously observed in the UV–Vis region, such as D and G-terms. These electronic transitions may be described based on Tanabe–Sugano diagrams [17]. In addition, different magnetic behaviors varying from ferro- to antiferromagnetic interactions of manganese (II) complexes were proven [18,19]. It is shown in the literature that inorganic–organic hybrid complexes play an important role in medicinal chemistry [20–22]. For instance, these components have wide application in drugs synthesis. Due to the emergence of antibiotic resistance, it is crucial to discover novel antibiotic classes [23]. In this regard, great efforts have been conducted with respect to the development of new hybrid compounds having antiparasitic, antimicrobial, anti-inflammatory, and anticancer properties [21,22,24].

In this paper, a new manganese (II) hybrid halide, $(C_5H_{14}N_2)[MnCl_4(H_2O)_2]$, possessing a zero dimensional structure is reported. The crystal structure, thermal behavior, spectroscopic characterization, and magnetic properties are presented. In addition, pharmacokinetic parameters of the compound units were assessed based on the absorption, distribution, metabolism, elimination, and toxicity (ADMET) attributes together with assessment of the antibacterial action.

2. Experimental Design

2.1. Materials and Synthesis

Sigma-Aldrich supplied the following commercially available raw ingredients to produce the desired chemical. Hexahydro-1,4-diazepine ($C_5H_{12}N_2$; 98%), Manganese(II) chloride ($MnCl_2$; 99%), and hydrochloric acid (HCl; 37%) were utilized without further purification.

The slow evaporation process was used to create the complex. By combining $MnCl_2$ (0.125 g, 1 mmol) and $(C_5H_{12}N_2)$ (0.100 g, 1 mmol) in 10 mL of distilled water, single crystals of the investigated chemical were produced from an aqueous solution. After that, 1 mL of strong HCl was added to the produced solution to make it acidic. A volume of 10 mL of distilled water was used to dissolve the mixture. The solution was magnetically agitated for 30 min, and then left to stand at room temperature. Seven days later, colorless crystals were produced and identified by single crystal X-ray diffraction.

2.2. X-ray Data Collection

A single crystal of the studied compound was glued and mounted at 150 K on a D8 VENTURE Bruker AXS diffractometer. Through the usage of the APEX 3 software, graphite monochromated Mo K radiation (with a wavelength of 0.71073) was employed. SAINT was used to process the data, including its collection, reduction, and analysis. The SADABS software was used to carry out the empirical absorption adjustments of the multi-scan kind. The crystal structure was determined to be in the monoclinic symmetry and the space group P2/c by using the automated search for space group offered in Wingx [25]. The molecular solid state structure was solved by direct methods using the SHELXT software package [26].

The graphite monochromated Mo $K\alpha$ radiation ($\lambda = 0.71073 \text{ \AA}$) was used through the program APEX 3. Data collection and reduction as well as their analysis were processed using SAINT. The SADABS program was used for the empirical absorption corrections

based on the automated search for space group available in Wingx [23], the crystal structure was solved in the monoclinic symmetry and the space group P2/c. The molecular solid state structure was solved by direct methods using the SHELXT software package [26]. On F2 with SHELXL-2015, it was improved using full-matrix least-square methods [27]. All non-hydrogen atoms were anisotropically refined. The hydrogen atoms that were O- and N-bonded were located using different maps, and they were then treated with Uiso (H) = 1.5 Uiso (O) and U (H) = 1.2 Uiso (N). Using software called DIAMOND, the drawings were created. Crystallographic data and the results of the least-squares structure refinement are given in Table S1.

2.3. Thermal Analysis

Thermal analysis was performed on powders using a TGA/DTA called the “SETSYS Evolution” under nitrogen flow (100 mL/min) and a heating rate of 5 °C min⁻¹ up to 600 °C (Pt crucibles, Al₂O₃ as a reference).

2.4. Spectroscopic Measurements

A Perkin Elmer 1650 FT-IR Spectro-photometer was used to obtain the infrared measurements. Diluted with spectroscopic KBr and pressed into a pellet, scans Samples were run on the range 500–4000 cm⁻¹.

At room temperature, optical absorption spectra of sample films were obtained using a typical UV-Vis absorption spectrometer (Hitachi, U-3300). The used wavelength ranged between 200 and 800 nm.

2.5. Magnetic Measurements

Magnetic data was recorded using a Quantum Design MPMS-XL SQUID magnetometer and Pascal's constants as previously reported [28].

2.6. Pharmacokinetics

The pharmacokinetic characteristics of the synthesized and described chemical units were examined using previously reported absorption, distribution, metabolism, excretion, and toxicity (ADMET) measures [24,29,30]. The bioavailability, which is primarily determined by physicochemical features such as flexibility (FLEX), insaturation (INSA), insolubility (INSO), lipophilicity (LIPO), molecular size (SIZE), and polarity (POLA), was also estimated [30–32].

2.7. Antimicrobial Activity

2.7.1. Microbial Strains

Six bacteria strains were used to investigate the antibacterial activity of (C₅H₁₄N₂)[MnCl₄(H₂O)₂]: three Gram-positive (*Listeria monocytogenes*, *Staphylococcus aureus*, and *Micrococcus luteus*) and three Gram-negative strains (*Salmonella typhi*, *Escherichia coli*, and *Enterococcus faecalis*).

2.7.2. Agar Diffusion Assay

Antibacterial activity was assessed using the Vanden Berghe technique [33]. The microorganisms were spread out on an LB medium at a concentration of 10⁶ colony forming units (CFU) mL⁻¹ of bacteria cell suspension. After being dissolved in DMSO and added (20 L) to wells punched in the agarose layer, (C₅H₁₄N₂)[MnCl₄(H₂O)₂] was allowed to diffuse in the layer and incubated for 3 h at 4 °C in a humid, close container. The examined microorganisms were cultured at 37 °C for 24 h after diffusion. Ampicillin and DMSO were used as positive and negative controls, respectively, for antibacterial activity. Three sample replications were used for all assays, and results were averaged.

2.7.3. Determination of the Minimum Inhibitory Concentration (MIC)

The sample's antibacterial effectiveness was evaluated against Gram (+) and Gram (−) bacterial strains. A microwell dilution method, as previously described by [34,35], was used to determine MIC values using 3-(4,5-dimethylthiazol-2-yl)-2,5-diphenyltetrazolium bromide. MIC values correspond to the lowest concentration that completely inhibits the growth of microorganisms (MTT). The suspensions were adjusted to 106 CFU/mL and the inoculum of each bacteria was created. In a 96-well plate, dilution series of the sample were created, ranging from 10 mg/mL to 0.02 mg/mL. DMSO was used as a negative control. Following a 24 h incubation period at 37 °C, each well in the plates received 25 µL of newly produced MTT (0.5 mg/mL). The medium's transformation to a purple tint after 30 min of incubation showed that the bacteria were physiologically active. All studies were performed in duplicate, and the MIC was determined as the point at which the MTT color did not change.

2.8. Anti-Lipase Activity Assay

The possibility of a direct interaction between a lipase and an inhibitor in an aqueous media and in the absence of a substrate was investigated using the lipase-inhibitor pre-incubation technique [36].

The lipase that was utilized was *Candida rugosa* Lipase Type VII (EC 3.1.1.3) from SIGMA.

A pH-Stat (Metrohm, Herisau, Switzerland) was used to titrimetrically evaluate the lipase activity test at pH 7.2 and 37 °C using an olive oil emulsion. One mol of fatty acid is emitted each minute by one lipase unit.

50 µL of lipase were pre-incubated for 1 h at room temperature with varying concentrations of DMSO dissolved $(C_5H_{14}N_2)[MnCl_4(H_2O)_2]$ to measure the lipase inhibitory activity. As mentioned above, 50 µL aliquots from the reaction sample were utilized to measure the remaining lipase activity. In each instance, control studies were conducted using the same amount of DMSO but without the subject substance. It was highlighted that the enzyme activity is unaffected by DMSO at final volume concentrations lower than 10%. When compared to the initial activity, which was evaluated without the inhibitor, the lipase inhibition (in %) was computed. To determine the lipase inhibitory activity, 50 µL of Lipase was pre-incubated for 1 h at room temperature with different concentrations of the DMSO dissolved $(C_5H_{14}N_2)[MnCl_4(H_2O)_2]$. Aliquots of 50 µL from the reaction sample were used to assess the residual lipase activity.

3. Results and Discussion

3.1. Crystal Structure of $(C_5H_{14}N_2)[MnCl_4(H_2O)_2]$

The title organic–inorganic hybrid compound $(C_5H_{14}N_2)[MnCl_4(H_2O)_2]$ crystallizes in the P2/c monoclinic space group. Figure 1 illustrates the asymmetric unit of the structure drawn with 50% probability thermal ellipsoids. The asymmetric unit of the structure includes two crystallographically independent isomers cis/trans- $[MnCl_4(H_2O)_2]$ and one deprotonated hexahydro-1,4-diazepinediium cation. In this structure, the two manganese cations Mn1 (wyckof site: 2e, 2) and Mn2 (wyckof site: 2f, 2) are situated in special positions on the twofold rotation axis at $x = 1, z = 3/4$ and $x = 1/2, z = 1/4$, respectively. Each MnII ion is surrounded by four chlorides ions and two water molecules. It is noteworthy that the manganese octahedra adopt two types of isomers: trans- $[MnCl_4(H_2O)_2]$ and cis- $[MnCl_4(H_2O)_2]$ (Figure 2). As seen in Figure 3, the atomic arrangement can be described by alternation of a discrete anionic moiety $[MnCl_4(H_2O)_2]^{2-}$ and organic layers $(C_5H_{14}N_2)^{2+}$ which develop along the [101] direction.

The antiperiplanar angle O1—Mn1—O1i value is 171.81 (10)° and the synclinal angle O11—Mn2—O11ii is equal to 85.60 (8)°. The measured bond lengths and angles are shown in Table S2. The organic cations, $(C_5H_{14}N_2)^{2+}$, are located in general positions. Both nitrogen centers in the hexahydro-1,4-diazepinediium cations are protonated to compensate the inorganic part negative charges. The values of C–C and C–N distances vary in the range of 1.510 (3)–1.520 (3) Å and in the range of 1.494 (3)–1.514 (3) Å while the values of the angles

C–N–C and N–C–C range from 115.12 (17) to 117.94 (16) and from 111.65 (18) to 114.34 (18)° respectively, and the C–C–C angle is equal to 115.40 (18)° (Table S2). These values of bond distances and angles are comparable to those given in other hybrids containing hexahydro-1,4-diazepinediium as organic matrix [37,38].

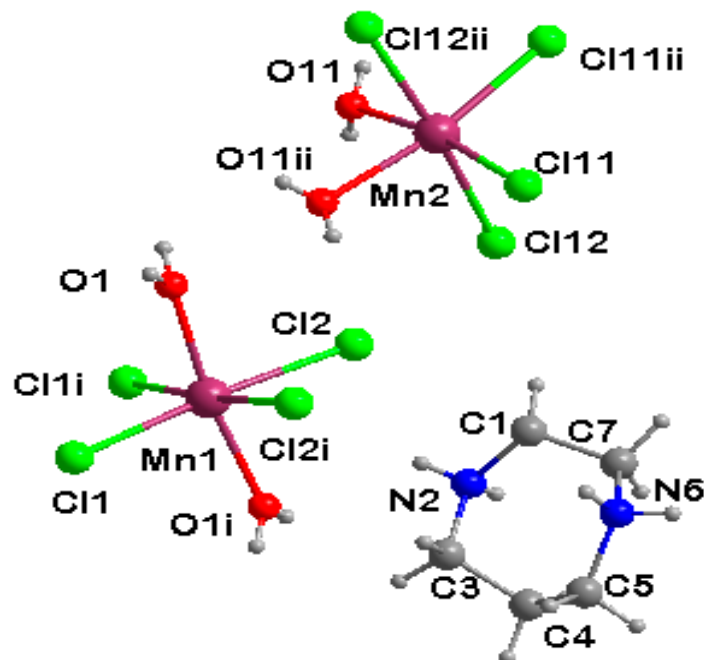


Figure 1. The asymmetric unit of $(C_5H_{14}N_2)[MnCl_4(H_2O)_2]$ (metal octahedron is completed by symmetry, symmetry code: (i) $-x + 1, y, -z + 1/2$; (ii) $-x + 2, y, -z + 3/2$).

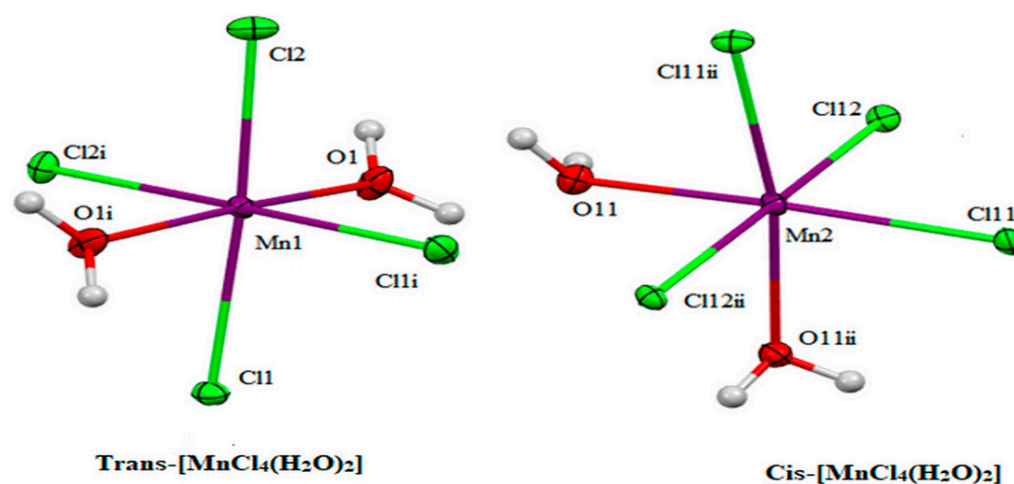


Figure 2. The isomers of $(C_5H_{14}N_2)[MnCl_4(H_2O)_2]$.

By forming N–H...O, N–H...Cl, and O–H...Cl hydrogen bonds with the organic and inorganic cations, water molecules and chloride ions contribute significantly to the stability of the crystal structure. The N...Cl distances inside the intermolecular bonds range between 3.203 (2) and 3.503 (2), whereas the O...Cl distances range from 3.118 (5) to 3.231 (5). The N...O distance is equal to 3.251 (3) (Table 1, Figure 3).

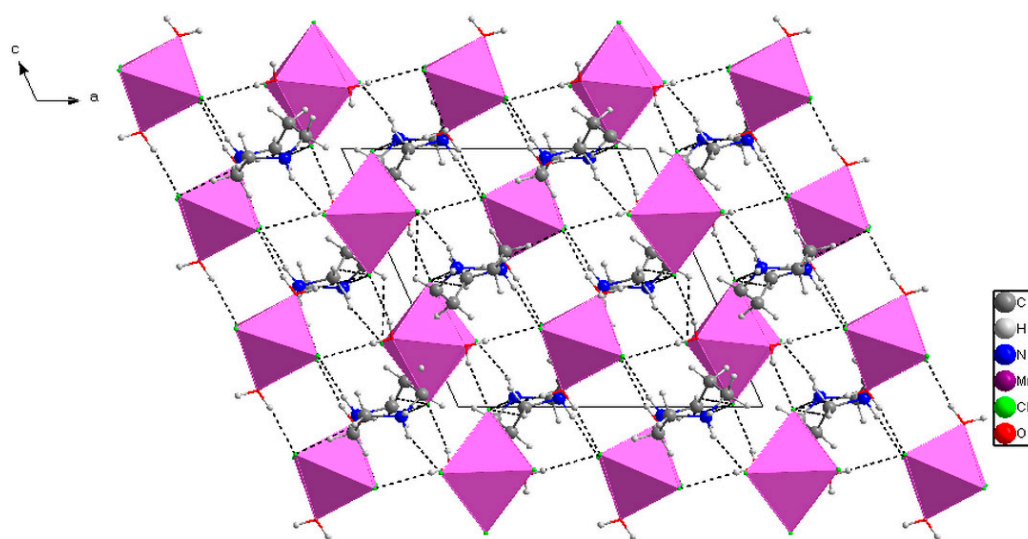


Figure 3. A view of the packing crystal of $(C_5H_{14}N_2)[MnCl_4(H_2O)_2]$ along the crystallographic b-axis.

Table 1. Intermolecular hydrogen bonds (\AA , $^\circ$) in $(C_5H_{14}N_2)[MnCl_4(H_2O)_2]$.

D—H...A	D—H	H...A	D...A	D—H...A
N2—H2A...Cl2 ⁱⁱⁱ	0.81 (3)	2.91 (3)	3.503 (2)	133 (3)
N2—H2A...Cl2 ^{iv}	0.81 (3)	2.71 (3)	3.3534 (19)	138 (3)
N2—H2A...O1 ⁱⁱⁱ	0.81 (3)	2.64 (3)	3.251 (3)	134 (3)
N2—H2B...Cl1	0.93 (3)	2.24 (3)	3.130 (2)	160 (3)
N6—H6A...Cl11 ^v	0.87 (3)	2.42 (3)	3.203 (2)	150 (2)
N6—H6B...Cl12 ^{vi}	0.89 (3)	2.38 (3)	3.258 (2)	168 (2)
O1—H1W1...Cl12	0.84 (3)	2.29 (3)	3.1310 (17)	179 (3)
O1—H1W2...Cl2 ^{iv}	0.88 (3)	2.29 (3)	3.1472 (18)	165 (3)
O11—H11A...Cl12 ^{vii}	0.77 (2)	2.55 (3)	3.3032 (17)	165 (3)
O11—H11B...Cl2 ^{vii}	0.81 (2)	2.44 (2)	3.2447 (17)	175 (3)

Symmetry codes: [(ⁱⁱⁱ) $-x + 1, -y + 1, -z + 1$; (^{iv}) $x, -y + 1, z + 1/2$; (^v) $-x + 1, y, -z + 3/2$; (^{vi}) $-x + 1, -y, -z + 1$; (^{vii}) $x - 1, -y, z - 1/2$].

3.2. Thermal Decomposition of $(C_5H_{14}N_2)[MnCl_4(H_2O)_2]$

Both thermogravimetric analysis and differential thermal analysis were used simultaneously to investigate the title compound's thermal stability (DTA). It was heated to a temperature between 10 and 600 °C in a platinum crucible at a rate of 5 °C/min. Figure 4 presents the findings. The TG curve suggests that this chemical is stable up to a temperature of roughly 80 °C. The loss of water molecules (theoretical loss, 9.36%) is the cause of the weight loss seen between 80 and 110 °C. Two endothermic peaks at 85 and 100 degrees Celsius on the DTA curve are present in conjunction with this event. The decomposition of the amine fragment and the loss of two chloride ions as HCl due to the atmospheric moisture, which most likely resulted in the formation of $MnCl_2$, are both responsible for the subsequent mass loss of 51% (theoretical loss, 50%), which occurred right after the complex was dehydrated and ended at 400 °C. On the DTA curve, this phenomenon is accompanied by two significant endothermic peaks at 210 and 222 °C.

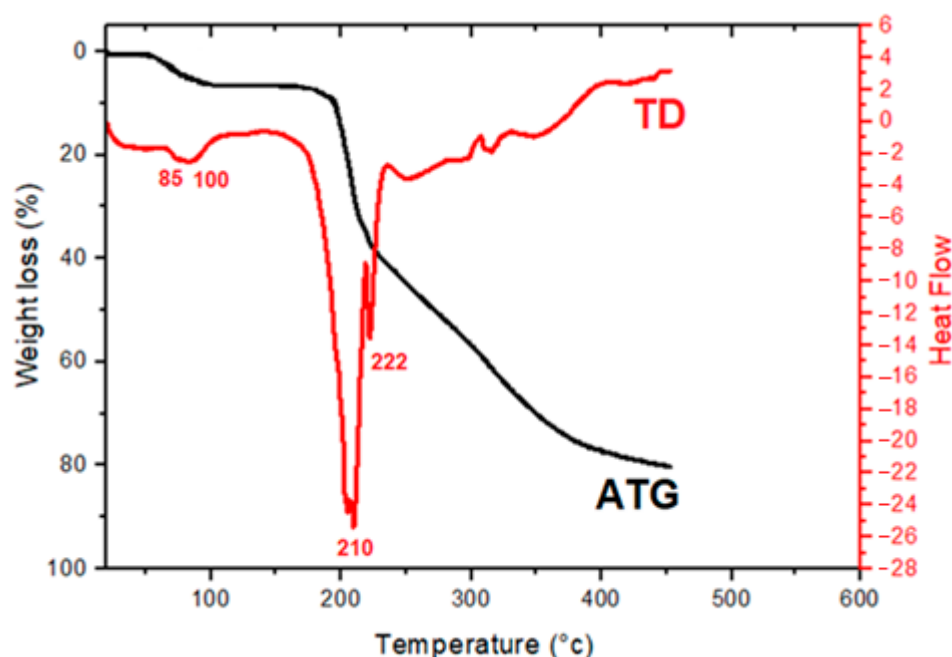


Figure 4. Simultaneous thermogravimetric analysis and differential thermal analysis scan for the decomposition of the title compound under flowing air with a heating rate of 10 °C/min between 25 and 500 °C.

3.3. Infrared Spectroscopy

Figure S1 exhibits the major selected absorptions in the IR spectra of compounds $(C_5H_{14}N_2)[MnCl_4(H_2O)_2]$ and their correspondent assignments, which associated with the hexahydro-1,4-diazepine molecule [37,39]. The results are displayed in Table S3. Indeed, NH_2 stretching vibrational modes have been situated in the wavenumbers range of $3051\text{--}3118\text{ cm}^{-1}$. The observed band at 2805 cm^{-1} is due to the CH_2 stretching modes. The band at 1647 cm^{-1} corresponds to NH_2 scissoring vibrations and that at 1570 cm^{-1} corresponds to δ_{as} (C-N-H) asymmetric bending. Frequencies in the range $1385\text{--}1450\text{ cm}^{-1}$ are associated to the $\delta(CH_2)$ scissoring vibrations. The bands which appear from 1103 to 1333 cm^{-1} can be assigned to the C-N stretching. The bands observed at 1021 and 1065 cm^{-1} are identified as C-C stretching modes. Moreover, the $\rho(NH_2)$ rocking modes is located at 976 cm^{-1} and the $\delta(C\text{--}C\text{--}C)$ scissoring mode is observed at 880 cm^{-1} . Furthermore, the vibrational bands situated at 529 and 780 cm^{-1} are assigned respectively to $\delta(C\text{--}N\text{--}C)$ and $\delta(C\text{--}C\text{--}N)$.

3.4. Optical Study

The optical properties of the material have an important potential to adapt to the needs of the technological components. The absorption spectrum can be seen in Figure 5. The intense band at 260 is attributed to electron charge transfers from the ligand to the metal LMCT. The bands from 300 to 500 nm should be ascribed to the electronic transitions between the ground and the first Mn^{2+} ion excited triplet states in the crystal field [40]. In addition, the electron transitions include two large distinct groups of absorption bands (D-terms and G-terms). Obviously, the bands of the D-terms exhibit stronger intensities than those of the G-terms. The absorption band at 322 and 364 nm can be assigned to the transitions from 6A_1 ground term to the ${}^4E(D)$ and ${}^4T_2(D)$ terms, respectively. The weak band, located at 430 nm, corresponds to the transition of the G-term ${}^6A_1 \rightarrow {}^4A_1, {}^4E(G)$ [17,40,41].

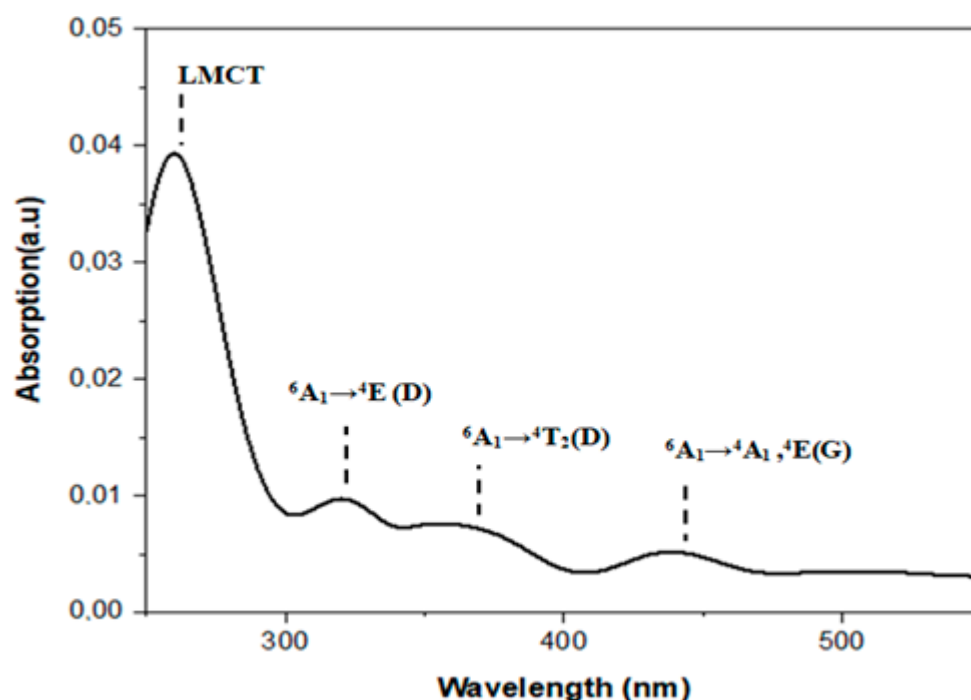


Figure 5. UV-Vis spectra of $(C_5H_{14}N_2)[MnCl_4(H_2O)_2]$.

The optical absorption coefficient (α) (cm^{-1}) can be determined using the relation of Beer–Lambert law [42]:

$$\alpha = 2.303A/d \quad (1)$$

where A and d (cm) are the absorbance and the thickness, respectively.

The energy of the incident photon is calculated using the equation:

$$h\nu = 1240/\lambda \text{ (nm)} \quad (2)$$

Generally, α is linked to the photon energy ($h\nu$) by the Tauc formula, which was expressed by the following equation [43].

$$\alpha h\nu = B (h\nu - E_g)^n \quad (3)$$

in which B is a constant reflecting the disorder degree of the crystal structure, h is Planck's constant, E_g represents the optical band gap, and n is the power factor which indicates the transition mode, $n = 2$ and $1/2$ for indirect and direct transitions, respectively. A plot of $(\alpha h\nu)^2$ and $(\alpha h\nu)^{1/2}$ versus $h\nu$ is shown in Figure 6A,B, respectively. The band gap determined by linear extrapolation of $(\alpha h\nu)^n$ to the zero absorption coefficient on the energy axis. The band gap energy for our compound is estimated to be 4.58 and 4.44 eV for $n = 1/2$ and $n = 2$, respectively. These values indicate that the title material can be classified as semi-conductor material.

The Eu behavior can describe the disorder degree and the defects of the structural connection of this material [44] according to the Urbach rule in the low photon energy range:

$$\ln(\alpha) = \ln(\alpha_0) + h\nu/E_u$$

where α is a constant and E_u is the Urbach energy that characterizes the exponential edge slope.

The inverse of the slope of the straight ($\ln(\alpha)$) versus ($h\nu$) deduced from the Figure 7 to the calculated value of E_u which estimated to 0.32 eV. This weak value of E_u energy confirms that this compound is ordered.

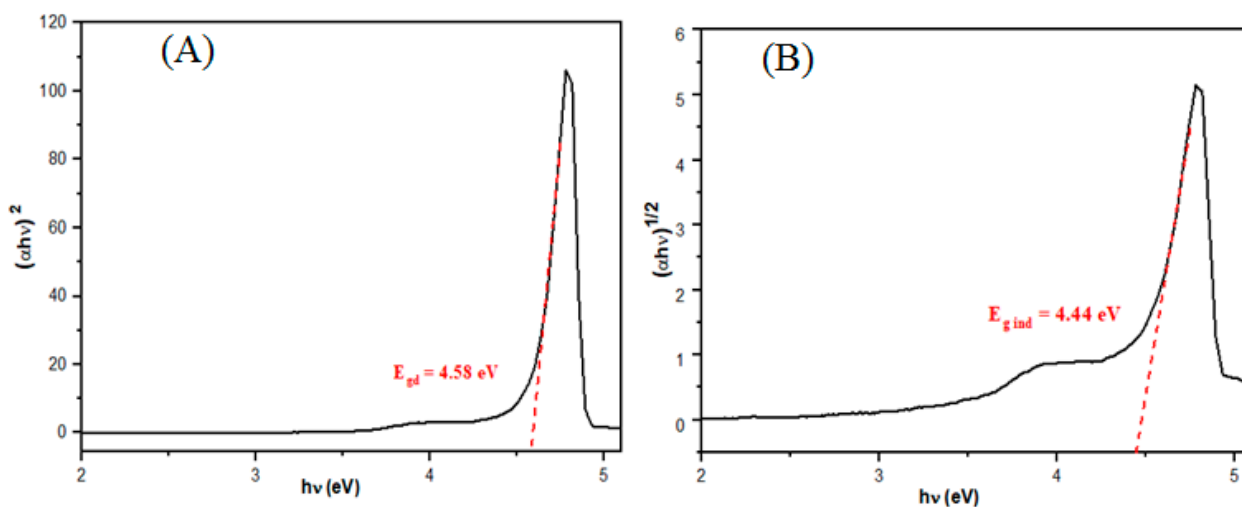


Figure 6. (A) Dependence of $(\alpha h\nu)^2$ and (B) $(\alpha h\nu)^{1/2}$ on the photon energy for the title compound.

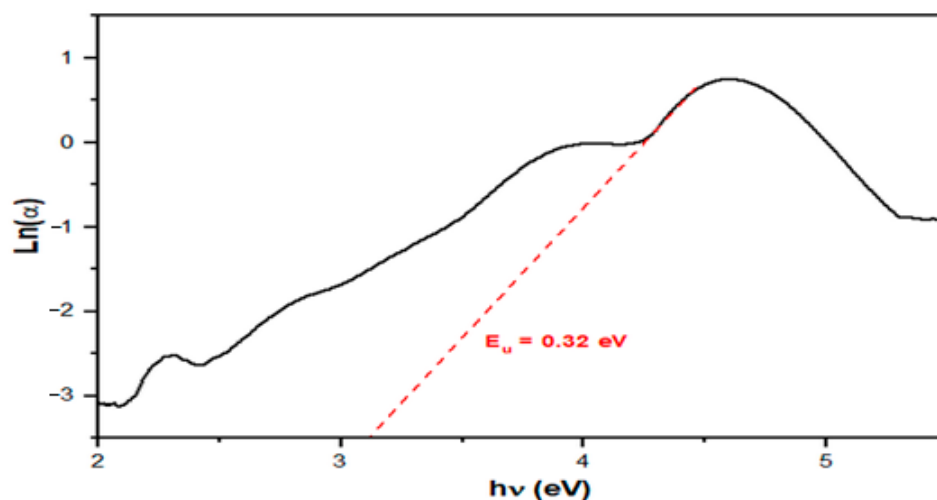


Figure 7. $\ln(\alpha)$ vs. photon energy (eV) of $(\text{C}_5\text{H}_{14}\text{N}_2)[\text{MnCl}_4(\text{H}_2\text{O})_2]$.

3.5. Magnetic Properties

The magnetization data as a function of field, M (H), at 1.8 K show that the magnetization is a linear relation up to approximately 1 T and then shows downward curvature up to 5 T nearly reaching saturation (Figure 8). The magnetization reaches a maximum of $\sim 28,000$ emu/mol confirmed the expected saturation magnetization of 28,375 emu/mol for $S = 5/2$ and $g = 2.00$.

The temperature dependence of χ_M measured for $(\text{C}_5\text{H}_{14}\text{N}_2)[\text{MnCl}_4(\text{H}_2\text{O})_2]$ over the temperature range 1.8–295 K and an applied field of 1000 Oe rises monotonically with decreasing temperature reaching a maximum of 1.03 emu/mol-Oe (Figure 9). Fitting of the χ_M^{-1} data from 10 K to 295 K to the Curie–Weiss law (Figure 10) gives a Curie constant = 4.405 (1) emu-K/mol-Oe and a Weiss constant, $\theta = -2.08$ (3) K, typical of an Mn(II) complex with negligible interactions [39]. θ is proportional to both S and J , [45] and therefore the small, negative value of θ indicates the presence of vanishingly weak antiferromagnetic interactions. The $\chi \cdot T$ product decreases at low temperatures, approaching a value 1.8 for our complex as T approaches 1.8 K. Given the very small interactions, it is unlikely that a unique magnetic lattice could be identified. However, the data were fit to the 1D-Heisenberg antiferromagnetic model to provide an estimate of the exchange which resulted in a Curie constant = 4.38 (2) emu-K/mol-Oe and $J = -0.15$ (1) K, including a fixed

1% paramagnetic impurity. Our findings paralleled those of Curie–Weiss fit and support the presence of very weak anti-ferromagnetic exchange between the Mn(II) ions.

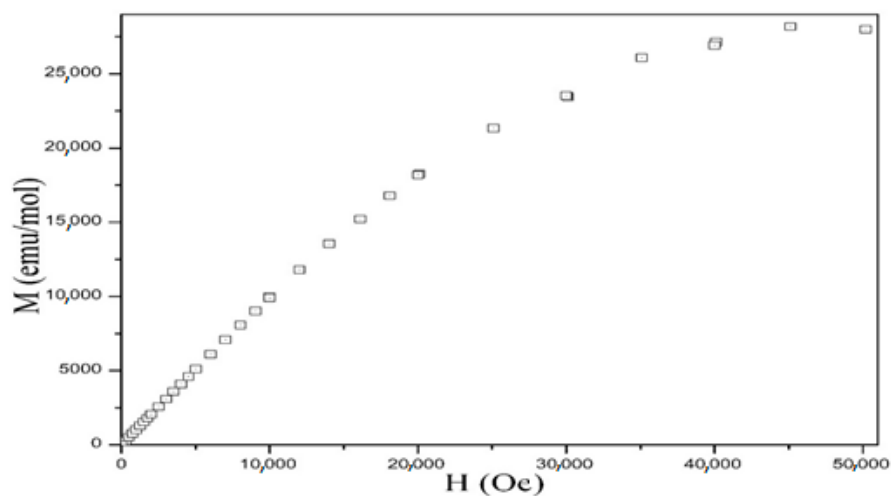


Figure 8. Field dependence of the magnetization at 1.8 K for $(\text{C}_5\text{H}_{14}\text{N}_2)[\text{MnCl}_4(\text{H}_2\text{O})_2]$.

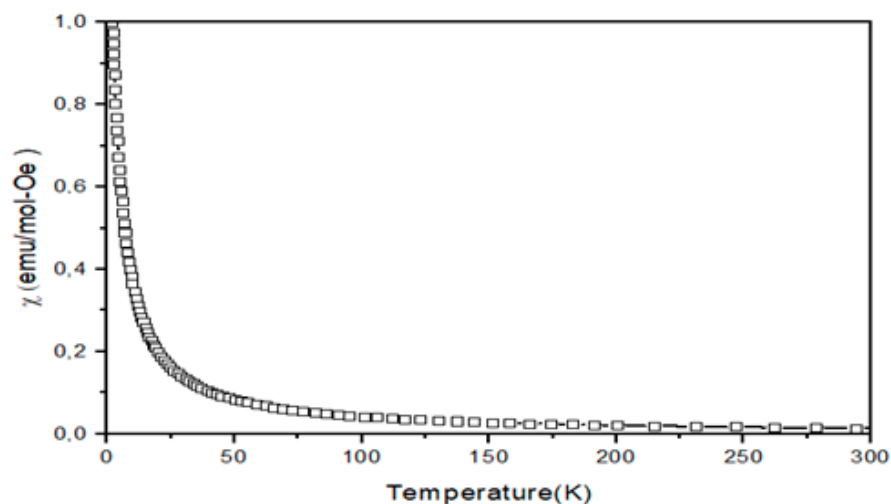


Figure 9. Plot of χ vs. temperature of $(\text{C}_5\text{H}_{14}\text{N}_2)[\text{MnCl}_4(\text{H}_2\text{O})_2]$.

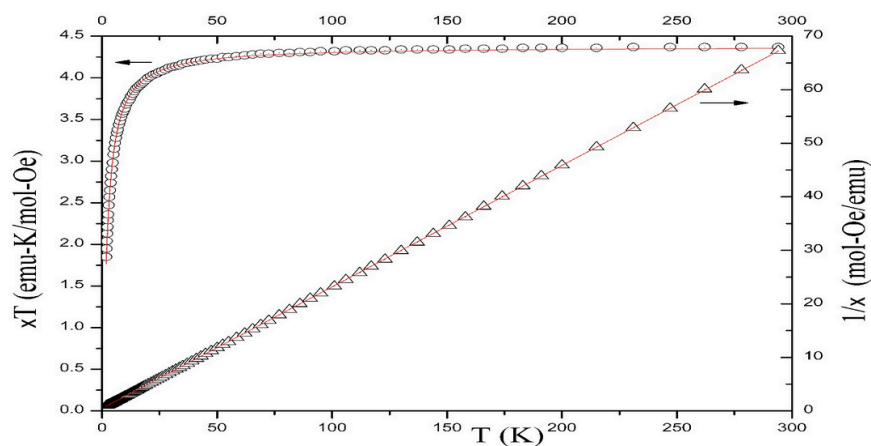


Figure 10. $\chi T(T)$ (o, left axis) and $\chi^{-1}(T)$ (Δ , right axis) in the temperature range from 1.8 to 300 K for $(\text{C}_5\text{H}_{14}\text{N}_2)[\text{MnCl}_4(\text{H}_2\text{O})_2]$. The solid red lines represent the Curie–Weiss fit of the data.

3.6. Biological Activities

3.6.1. Bioavailability and Pharmacokinetic Findings

The pharmacokinetic findings are exhibited by Table 2 and Figure 11. It was found that the two isomers Cis/Trans of $[\text{MnCl}_4(\text{H}_2\text{O})_2]$ possessed similar bioavailability and pharmacokinetics properties.

Table 2. Lipophilicity, druglikeness, pharmacokinetics, and medicinal chemistry of 1 based on ADMET (for absorption, distribution, metabolism, excretion, and toxicity) properties.

Entry	1		
	Unit 1 ($\text{C}_5\text{H}_{14}\text{N}_2$)	Unit 2 ($\text{MnCl}_4(\text{H}_2\text{O})_2$)	
Lipophilicity/ Druglikeness	TPSA (\AA^2)	24.06	40.46
	Consensus Log Po/w	0.14	0.14
	Lipinski's Rule	Yes	Yes
	Bioavailability Score	0.55	0.55
Pharmacokinetics/ Medicinal Chemistry	GI absorption	Low	Low
	BBB permeant	No	No
	P-gp substrate	No	No
	CYP1A2 inhibition	No	No
	CYP2C19 inhibition	No	No
	CYP2C9 inhibition	No	No
	CYP2D6 inhibition	No	No
	CYP3A4 inhibition	No	No
	Log Kp (cm/s)	-7.27	-7.27
	Leadlikeness	No	No
	Synthetic accessibility	1.43	1.43

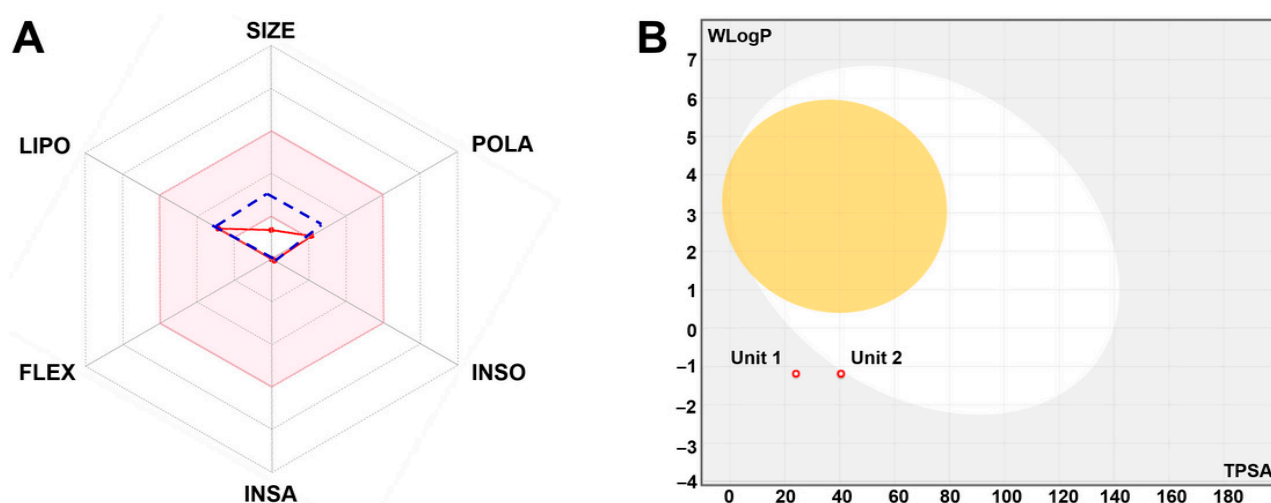


Figure 11. Bioavailability hexagon of the synthesized compound (A) and its boiled-egg model (B) based on its physico-chemical parameters: Molecular size (SIZE), lipophilicity (LIPO), insolubility (INSO), insaturation (INSA), polarity (POLA) and flexibility (FLEX). Unit 1 and 2 represent the $\text{C}_5\text{H}_{14}\text{N}_2$ and Cis/Trans of $\text{MnCl}_4(\text{H}_2\text{O})_2$ parts of the compound.

Such data are commonly assessed in drug management and design to avoid any drug failure at advanced stages [24,30,32]. As indicated in the Table 2, the hybrid compound

units have acceptable bioavailability, which indicates the potential physiological activity without toxic outcomes as both meet the Lipinski rule [31,32]. The compound units are associated with low gastro-intestinal (GI) absorption and blood–brain barrier (BBB) permeation, which was supported by the boiled-egg model. While both units inhibited none of the major cytochrome P450 (CYP) isoforms (1A2, C19, 2C9, 2D6, and 3A4), it was expected to not behave as P-glycoprotein (P-gp) substrates. Thus, it could be deduced that the complex may not disrupt the distribution, metabolism, and elimination of drugs. Log K_p calculation, as assessed using both lipophilicity and molecular weight, resulted in low skin permeability [46]. Regarding, synthetic accessibility, it was deduced that the complex presented average ease to synthesize once compared with other synthesized and/or natural compounds with significant biological activities [24,30,46].

3.6.2. Antimicrobial Activity

The increase in drug-resistant pathogens is recently raising an urgent need to identify and isolate new bioactive compounds from different sources through modern, standardized analytical procedures [47]. In this line, the antibacterial activity of (C₅H₁₄N₂)[MnCl₄(H₂O)₂] was checked against Gram-positive (*L. monocytogenes*, *M. luteus*, *S. aureus*) and Gram-negative (*E. coli*, *E. faecalis*, *S. typhi*) bacteria. Using the agar diffusion method, antibacterial activity was determined by measuring both the clear zone of growth inhibition diameter and the MIC values (mg/L). Table 3, the title compound showed various degrees of antibacterial activity against Gram-positive and Gram-negative strains. MIC values ranged between 6 and 20 mm using 1 and 2 mg/mL of (C₅H₁₄N₂)[MnCl₄(H₂O)₂], respectively. The micro well dilution method, used in order to determine with precision the MIC, showed a dose-dependent antibacterial activity of the studied compound with a MIC 2.5 mg/mL. This inhibitory effect can be explained by the interaction between (C₅H₁₄N₂)[MnCl₄(H₂O)₂] and bacterial membrane compound. In fact, the integrity of the bacterial plasmic membrane is responsible for osmoregulation, respiration, biosynthesis, and reticulation of peptidoglycan, as well as lipid biosynthesis. The bacterial plasma membrane disruption can directly or indirectly cause metabolic dysfunction and finally lead to bacterial death [48].

Table 3. Antibacterial activities of 1. MIC (mg/mL), Inhibition zones: +++: >15 mm; ++: 5–15 mm, +: <5 mm.

Bacterial Strain	Gram	Inhibition Zone Diameter (mm)		MIC (mg/mL)
		1 mg/mL	2 mg/mL	
<i>Escherichia coli</i>	-	+	+	1
<i>Enterococcus faecalis</i>	-	+	+	1
<i>Salmonella typhi</i>	-	+	+	1.3
<i>Listeria monocytogenes</i>	+	++	+++	2.5
<i>Staphylococcus aureus</i>	+	++	+++	2.5
<i>Micrococcus luteus</i>	+	++	+++	2.5

3.6.3. Anti-Lipase Activity

Lipases are triacylglycerol ester hydrolases (EC 3.1.1.3), which catalyze the hydrolysis of long-chain triglycerides. These enzymes act at the aqueous–organic interface to catalyze the hydrolysis of ester bonds present in carboxylases, releasing organic acid glycerides and glycerol [49]. It has been reported that microbial pathogens produced several lipases, which play a key role in the development of infectious [35,50] and metabolic diseases [51,52]. Thus, research on novel lipase inhibitors for the treatment of such diseases has gained a high interest during the last decade. Therefore, we evaluate the inhibitory effect of the studied compound toward lipase and using *Candida rugosa* lipase as model.

Candida rugosa lipase was inhibited in a dose dependent manner with (C₅H₁₄N₂)[MnCl₄(H₂O)₂] increased concentrations. Figure 12 presents the linear kinetics corresponding to the Free Fatty Acids (μmol) released vs. (C₅H₁₄N₂)[MnCl₄(H₂O)₂] amount

(mg). At 3 mg, the sample showed 50% inhibition of the lipase activity, while at 5 mg, the inhibition effect reached 97%. This inhibition can be explained by covalently or non-covalently interaction between $(C_5H_{14}N_2)[MnCl_4(H_2O)_2]$ with amino acids of the lipase active site, as previously reported by several published molecular interactions modeling [53–55]. As this compound showed promising biological effects, further investigations would confirm the current findings and support the potential pharmacological use of $(C_5H_{14}N_2)[MnCl_4(H_2O)_2]$ by the pharmaceutical companies.

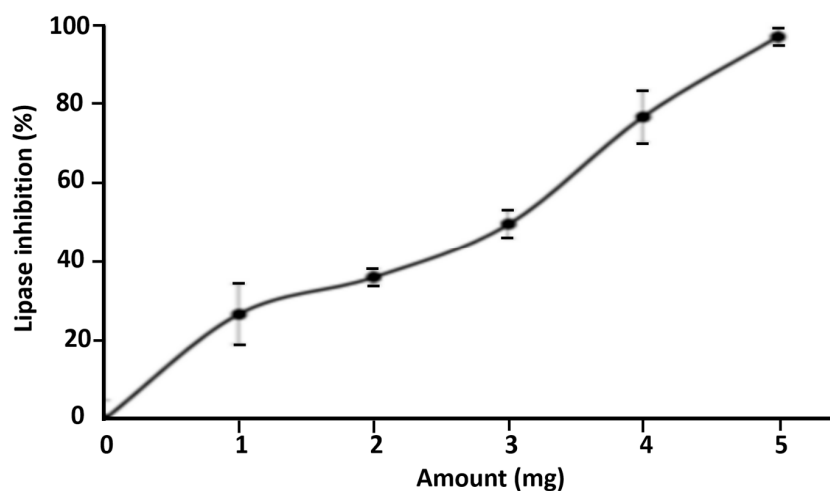


Figure 12. Evaluation of the inhibitory effect of the $(C_5H_{14}N_2)[MnCl_4(H_2O)_2]$ against *Candida rugosa* lipase. The enzyme was pre-incubated in the presence of various $(C_5H_{14}N_2)[MnCl_4(H_2O)_2]$ amounts for 1 h at 25 °C and the inhibition percentage was assessed.

4. Conclusions

In the current study, we synthesized and characterized a new hybrid compound $(C_5H_{14}N_2)[MnCl_4(H_2O)_2]$. The X-ray diffraction analysis shows that the basic unit structure of this compound consists of one $[C_5H_{14}N_2]^{2+}$ cation and two crystallographically inequivalent isomers Cis/Trans $[MnCl_4(H_2O)_2]^{2-}$. This hybrid material exhibits a layered inorganic–organic structure stabilized through N/O–H...Cl and N–H...O hydrogen bonding between the inorganic and organic moieties, causing the formation of a three-dimensional supramolecular architecture. The thermal decomposition of the crystals proceeded through two stages, giving rise to manganese (II) dichloride as endpoint compound. IR spectroscopy was applied to confirm the presence of various functional groups in the crystal. Optical parameters were obtained using UV–Vis absorption. The band gap energy demonstrates that the compound can be classified as a semi-conductor material. The low value of Urbach energy indicates that the material is ordered. The variable temperature magnetic susceptibility data indicate very weak antiferromagnetic interactions. Additionally, the present study emphasized the significant role attributed to $(C_5H_{14}N_2)[MnCl_4(H_2O)_2]$ as a promising source of antibacterial and antilipase activities. These potential effects have been confirmed by both bioavailability and the pharmacokinetic analyses.

Supplementary Materials: The following supporting information can be downloaded at: <https://www.mdpi.com/article/10.3390/inorganics11020076/s1>, Table S1: Crystal data and structure refinement for $(C_5H_{14}N_2)[MnCl_4(H_2O)_2]$, Table S2: Main distances (Å) and angles (°) for $(C_5H_{14}N_2)[MnCl_4(H_2O)_2]$ atomic arrangement, Table S3: Observed vibration frequencies (cm^{-1}) and band assignments for $(C_5H_{14}N_2)[MnCl_4(H_2O)_2]$, Figure S1: Infrared absorption spectra of the studied compound. CCDC 2214720 contains the supplementary crystallographic data for this paper. These data can be obtained free of charge via www.ccdc.cam.ac.uk/data_request/cif, by emailing data_request@ccdc.cam.ac.uk, or by contacting The Cambridge Crystallographic Data Centre, 12 Union Road, Cambridge CB2 1EZ, UK; fax: +44(0)1223-336033.

Author Contributions: Conceptualization, R.B. and H.N.; data curation, S.W. and M.S.; formal analysis, W.M.A.; funding acquisition, R.B.; investigation, F.B. and T.R.; methodology, M.B., S.W. and W.M.A.; project administration, R.B.; resources, N.K. and M.M.T.; software, R.B.; validation, F.B., M.S. and T.R.; writing—original draft, M.B.; writing—review and editing, R.B. and H.N. All authors have read and agreed to the published version of the manuscript.

Funding: This research has been funded by the Deanship of Scientific Research at University of Ha'il—Saudi Arabia through project number GR-22 059.

Data Availability Statement: The data presented in this study are available in the article and its supplementary materials.

Acknowledgments: This research has been funded by Scientific Research Deanship at University of Ha'il—Saudi Arabia through project number GR-22 059.

Conflicts of Interest: The authors declare no conflict of interest.

References

1. Dolbecq, A.; Dumas, E.; Mayer, C.R.; Mialane, P. Hybrid organic–inorganic polyoxometalate compounds: From structural diversity to applications. *Chem. Rev.* **2010**, *110*, 6009–6048. [[CrossRef](#)]
2. Allen, F.H.; Hoy, V.J.; Howard, J.A.; Thalladi, V.R.; Desiraju, G.R.; Wilson, C.C.; McIntyre, G.J. Crystal engineering and correspondence between molecular and crystal structures. Are 2- and 3-aminophenols anomalous. *J. Am. Chem. Soc.* **1997**, *119*, 477–3480. [[CrossRef](#)]
3. Sanchez, C.; Julián, B.; Belleville, P.; Popall, M. Applications of hybrid organic–inorganic nanocomposites. *J. Mat. Chem.* **2005**, *15*, 3559–3592. [[CrossRef](#)]
4. Sayer, I.; Dege, N.; Ghalla, H.; Moliterni, A.; Naili, H. Crystal structure, DFT studies and thermal characterization of new luminescent stannate (IV) based inorganic-organic hybrid compound. *J. Mol. Struct.* **2021**, *1224*, 129–266. [[CrossRef](#)]
5. Hfidhi, N.; Bkhairia, I.; Atoui, D.; Boonmak, J.; Nasri, M.; Salem, R.B.; Youngme, S.; Naili, H. Catalytic and biological valorization of a supramolecular mononuclear copper complex based 4-aminopyridine. *Appl. Organomet. Chem.* **2019**, *33*, 4793. [[CrossRef](#)]
6. Nicole, L.; Laberty-Robert, C.; Rozes, L.; Sanchez, C. Hybrid materials science: A promised land for the integrative design of multifunctional materials. *Nanoscale* **2014**, *6*, 6267–6292. [[CrossRef](#)] [[PubMed](#)]
7. Ye, B.H.; Tong, M.; Chen, X. Metal-organic molecular architectures with 2, 2'-bipyridyl-like and carboxylate ligands. *Coord. Chem. Rev.* **2005**, *249*, 545–565. [[CrossRef](#)]
8. Bu, X.H.; Tong, M.; Chang, H.; Kitagawa, S.; Batten, S. A Neutral 3D Copper Coordination Polymer Showing 1D Open Channels and the First Interpenetrating NbO-Type Network. *Angew. Chem. Int. Ed.* **2004**, *43*, 192–195. [[CrossRef](#)]
9. Gómez, V.; Corbella, M. Crystal Structure and Magnetic Properties of the Dinuclear MnII Compound [Mn₂(bpy)₄(2-CIC₆H₄COO)₂](ClO₄)₂EtOH. *J. Chem. Crystallogr.* **2011**, *41*, 843–846. [[CrossRef](#)]
10. Pardasani, R.T.; Pardasani, P. Molar magnetic moment of manganese (II) complex with phosphate Schiff-base, In Magnetic Properties of Paramagnetic Compounds. *Magn. Susceptibility Data* **2021**, *1*, 702–703.
11. Zhang, S.; Zhao, Y.; Zhou, J.; Ming, H.; Wang, C.H.; Jing, X.; Zhang, Q. Structural design enables highly-efficient green emission with preferable blue light excitation from zero-dimensional manganese (II) hybrids. *J. Chem. Eng.* **2021**, *421*, 129886. [[CrossRef](#)]
12. Liu, Y.; Zhang, J.; Han, B.; Wang, X.; Wang, Z.; Xue, C.; Wu, T. New insights into Mn–Mn coupling interaction-directed photoluminescence quenching mechanism in Mn²⁺-doped semiconductors. *J. Am. Chem. Soc.* **2020**, *142*, 6649–6660. [[CrossRef](#)] [[PubMed](#)]
13. Morad, V.; Cherniukh, I.; Pötschacher, L.; Shynkarenko, Y.; Yakunin, S.; Kovalenko, M.V. Manganese (II) in tetrahedral halide environment: Factors governing bright green luminescence. *Chem. Mater.* **2019**, *31*, 10161–10169. [[CrossRef](#)] [[PubMed](#)]
14. Jiang, B.; Chi, F.; Zhao, L.; Wei, X.; Chen, Y.; Yin, M. Luminescence properties of a new green emitting long afterglow phosphor Ca₁₄Zn₆Ga₁₀O₃₅: Mn²⁺, Ge⁴⁺. *J. Lumin.* **2019**, *206*, 234–239. [[CrossRef](#)]
15. Mhadhbi, N.; Dgachi, S.; Belgacem, S.; Ben Ahmed, A.; Henry, N.; Loiseau, T.; Nasr, S.; Badraoui, R.; Naili, H. Design, theoretical study, druggability, pharmacokinetics and properties evolution of a new organo-bromocadmate compound as prospective anticancer agent. *J. Mol. Struct.* **2023**, *1274*, 134439. [[CrossRef](#)]
16. Drzewiecki, A.; Padyak, B.; Adamiv, V.; Burak, Y.; Teslyuk, I. EPR spectroscopy of Cu²⁺ and Mn²⁺ in borate glasses. *Nukleonika* **2013**, *58*, 379–385.
17. Chen, J.; Zhang, Q.; Zheng, F.K.; Liu, Z.F.; Wang, S.H.; Wu, A.Q.; Guo, G.C. Intense photo- and tribo-luminescence of three tetrahedral manganese (II) dihalides with chelating bidentate phosphine oxide ligand. *Dalton Trans.* **2015**, *44*, 3289–3294. [[CrossRef](#)]
18. Zhai, B.; Song, L.L.; Wang, W.J.; Li, Z.Y.; Li, S.Z.; Zhang, F.L.; Zang, Y.B. Structures and magnetic properties of 3D manganese (II)- and 2D pillar-layered copper (II)-organic framework derived from mixed carboxylate ligands. *J. Solid State Chem.* **2018**, *264*, 29–34. [[CrossRef](#)]
19. Li, C.; Bai, X.; Guo, Y.; Zou, B. Tunable emission properties of manganese chloride small single crystals by pyridine incorporation. *ACS Omega*. **2019**, *4*, 8039–8045. [[CrossRef](#)] [[PubMed](#)]

20. Derbel, M.A.; Jlassi, R.; Roisnel, T.; Badraoui, R.; Krayem, N.; Al-Ghulikah, H.; Rekik, W.; Naili, H. The effect of partial substitution of chloride by bromide in the 0-D hybrid material (C₄H₁₂N₂)[CuCl₄]·2H₂O: Structural, vibrational, thermal, in silico and biological characterizations. *J. Coordination Chem.* **2022**, *75*, 2628–2645. [[CrossRef](#)]
21. Jabeur, W.; Korb, M.; Al-Otaibi, J.; Čižmár, E.; Badraoui, R.; Zeleňák, V.; Naili, H. Physico-chemical characterizations and Biological evaluation of a new semiconducting metal-organic compound based on pyrimidine frameworks. *Inorg. Chem. Commun.* **2022**, *139*, 109279. [[CrossRef](#)]
22. Hchicha, K.; Korb, M.; Badraoui, R.; Naili, H. A novel sulfate-bridged binuclear copper (II) complex: Structure, optical, ADMET and in vivo approach in a murine model of bone metastasis. *New J. Chem.* **2021**, *45*, 13775–13784. [[CrossRef](#)]
23. Singh, K.; Kumar, Y.; Puri, P.; Sharma, C.; Aneja, K.R. Antimicrobial, spectral and thermal studies of divalent cobalt, nickel, copper and zinc complexes with triazole Schiff bases. *Arab. J. Chem.* **2017**, *10*, S978–S987. [[CrossRef](#)]
24. Mhadhbi, N.; Issaoui, N.; Hamadou, W.S.; Jahoor, M.A.; Elhadi, A.S.; Adnan, M.; Naiotali, H.; Badraoui, R. Physico-Chemical Properties, Pharmacokinetics, Molecular Docking and In-Vitro Pharmacological Study of a Cobalt(II) Complex Based on 2-Aminopyridine. *ChemistrySelect* **2022**, *7*, 103592.
25. Farrugia, L.J. WinGX and ORTEP for Windows: An update. *J. Appl. Crystallogr.* **2012**, *45*, 849–854. [[CrossRef](#)]
26. Sheldrick, G. ShelXT-Integrated space-group and crystal-structure determination. *Acta Cryst.* **2015**, *71*, 3–9. [[CrossRef](#)] [[PubMed](#)]
27. Sheldrick, G.M. Crystal structure refinement with SHELXL. *Acta Crystallogr. C Struct. Chem.* **2015**, *71*, 3–8. [[CrossRef](#)]
28. Macek, L.; Bellmay, J.C.; Faber, K.; Milson, C.R.; Landee, C.P.; Dickie, D.A.; Turnbull, M.M. Transition of halide complexes of 4'-aminoacetophenone: Synthesis, structures, and magnetic behavior. *Polyhedron* **2023**, *229*, 116214. [[CrossRef](#)]
29. Zammel, N.; Jedli, O.; Rebai, T.; Hamadou, W.S.; Elkahoui, S.; Jamal, A.; Alam, J.A.; Adnan, M.; Siddiqui, A.J.; Alreshidi, M.M.; et al. Kidney injury and oxidative damage alleviation by *Zingiber officinale*: Pharmacokinetics and protective approach in a combined murine model of osteoporosis. *3 Biotech* **2022**, *12*, 112. [[CrossRef](#)]
30. Badraoui, R.; Saeed, M.; Bouali, N.; Hamadou, W.S.; Elkahoui, S.; Alam, M.J.; Siddiqui, A.J.; Adnan, M.; Saoudi, M.; Rebai, T. Expression profiling of selected immune genes and trabecular microarchitecture in breast cancer skeletal metastases model: Effect of α -tocopherol acetate supplementation. *Calcif. Tissue Int.* **2022**, *110*, 475–488. [[CrossRef](#)]
31. Jedli, O.; Ben-Nasr, H.; Zammel, N.; Rebai, T.; Saoudi, M.; Elkahoui, S.; Jamal, A.; Siddiqui, A.J.; Sulieman, A.E.; Alreshidi, M.M.; et al. Attenuation of ovalbumin-induced inflammation and lung oxidative injury in asthmatic rats by *Zingiber officinale* extract: Combined in silico and in vivo study on antioxidant potential, STAT6 and TNF- α pathways. *3 Biotech* **2022**, *12*, 3249. [[CrossRef](#)]
32. Badraoui, R.; Saoudi, M.; Hamadou, W.S.; Elkahoui, S.; Siddiqui, A.J.; Alam, J.M.; Jamal, A.; Adnan, M.; Sulieman, A.M.E.; Alreshidi, M.M.; et al. Antiviral effects of Artemisinin and its derivatives against SARS-CoV-2 main protease: Computational evidences and interactions with ACE2 allelic variants. *Pharmaceuticals* **2022**, *15*, 129. [[CrossRef](#)] [[PubMed](#)]
33. Vanden Berghe, D. Screening methods for antibacterial and antiviral agents from higher plants. *J. Plant Biochem.* **1991**, *6*, 47–69.
34. Melo, M.; Feitosa, J.; Freitas, A.; De Paula, R. Isolation and characterization of soluble sulfated polysaccharide from the red seaweed *Gracilaria cornea*. *Carbohydr. Polym.* **2002**, *49*, 491–498. [[CrossRef](#)]
35. Noumi, E.; Snoussi, M.; Anouar, E.H.; Alreshidi, M.; Veettil, V.N.; Elkahoui, S.; Adnan, M.; Patel, M.; Kadri, A.; Aouadi, K.; et al. HR-LCMS-Based Metabolite Profiling, Antioxidant, and Anticancer Properties of *Teucrium polium* L. Methanolic Extract: Computational and In Vitro Study. *Antioxidants* **2020**, *9*, 1089. [[CrossRef](#)] [[PubMed](#)]
36. Lengsfeld, H.; Beaumier-Gallon, G.; Chahinian, H.; De Caro, A.; Verger, R.; Laugier, R.; Carrière, F. Physiology of gastrointestinal lipolysis and therapeutic use of lipases and digestive lipase inhibitors, Lipases and Phospholipases in Drug Development. *Biochem. Pharmacol.* **2004**, *195*–229.
37. Said, M.; Boughzal, H. Structural characterization and physicochemical features of new coordination polymer homopiperazine-1, 4-dium tetrachlorocadmate (II). *J. Mol. Struct.* **2020**, *1220*, 128696. [[CrossRef](#)]
38. Shi, Q.Z.; Xing, Z.; Cao, Y.N.; Ma, S.B.; Chen, L.Z. Synthesis, structure and dielectric properties of a Cd coordination polymer based on homopiperazine. *J. Mol. Struct.* **2017**, *1130*, 363–367. [[CrossRef](#)]
39. Bourwina, M.; Msalmi, R.; Walha, S.; Turnbull, M.M.; Roisnel, T.; Costantino, F.; Naili, H. A new lead-free 1D hybrid copper perovskite and its structural, thermal, vibrational, optical and magnetic characterization. *J. Mat. Chem C* **2021**, *9*, 5970–5976. [[CrossRef](#)]
40. Bai, X.; Zhong, H.; Chen, B.; Chen, C.; Han, J.; Zeng, R.; Zou, B. Pyridine-modulated Mn ion emission properties of C₁₀H₁₂N₂MnBr₄ and C₅H₆NMnBr₃ single crystals. *J. Phy. Chem C* **2018**, *122*, 3130–3137. [[CrossRef](#)]
41. Qaid, S.M.; Al-Asbahi, B.A.; Ghaithan, H.M.; AlSalhi, M.S. Optical and structural properties of CsPbBr₃ perovskite quantum dots/PFO polymer composite thin films. *J. Colloid Interface Sci.* **2020**, *563*, 426–434. [[CrossRef](#)] [[PubMed](#)]
42. Tauc, J. (Ed.) *Amorphous and Liquid Semiconductors*; Springer Science & Business Media: Boston, MA, USA, 2012.
43. Gagandeep; Singh, K.; Lark, B.S.; Sahota, H.S. Attenuation measurements in solutions of some carbohydrates. *Nucl. Sci. Eng.* **2000**, *134*, 208–217. [[CrossRef](#)]
44. Studenyak, I.; Kranjčec, M.; Kurik, M. Urbach rule in solid state physics. *Int. J. Opt. Appl.* **2014**, *4*, 76–83.
45. Landee, C.P.; Turnbull, M.M. A gentle introduction to magnetism: Units, fields, theory, and experiment. *J. Coord. Chem.* **2014**, *67*, 375–439. [[CrossRef](#)]
46. Badraoui, R.; Adnan, M.; Bardakci, F.; Alreshidi, M.M. Chloroquine and hydroxychloroquine interact differently with ACE2 domains reported to bind with the coronavirus spike protein: Mediation by ACE2 Polymorphism. *Molecules* **2021**, *26*, 673. [[CrossRef](#)]

47. Vaou, N.; Stavropoulou, E.; Voidarou, C.; Tsigalou, C.; Bezirtzoglou, E. Towards advances in medicinal plant antimicrobial activity: A review study on challenges and future perspectives. *Microorganisms* **2021**, *9*, 2041. [[CrossRef](#)] [[PubMed](#)]
48. Hartmann, M.; Berditsch, M.; Hawecker, J.; Ardakani, M.F.; Gerthsen, D.; Ulrich, A.S. Damage of the bacterial cell envelope by antimicrobial peptides gramicidin S and PG La as revealed by transmission and scanning electron microscopy. *Antimicrob. Agents Chemother.* **2010**, *54*, 3132–3142. [[CrossRef](#)] [[PubMed](#)]
49. de Morais Junior, W.G.; Kamimura, E.S.; Ribeiro, E.; Pessela, B.C.; Cardoso, V.L.; de Resende, M.M. Optimization of the production and characterization of lipase from *Candida rugosa* and *Geotrichum candidum* in soybean molasses by submerged fermentation. *Protein Expr. Purif.* **2016**, *123*, 26–34. [[CrossRef](#)] [[PubMed](#)]
50. Ruiz, C.; Falcocchio, S.; Xoxi, E.; Villo, L.; Nicolosi, G.; Pastor, F.; Diaz, P.; Saso, L. Inhibition of *Candida rugosa* lipase by saponins, flavonoids and alkaloids. *J. Mol. Catal. B Enzym.* **2006**, *40*, 138–143. [[CrossRef](#)]
51. Badraoui, R.; Ben-Nasr, H.; Bardakçi, F.; Rebai, T. Pathophysiological impacts of exposure to an endocrine disruptor (tetradifon) on α -amylase and lipase activities associated metabolic disorders. *Pestic. Biochem. Physiol.* **2020**, *167*, 104606. [[CrossRef](#)] [[PubMed](#)]
52. Badraoui, R.; Sahnoun, Z.; Abdelmoula, N.B.; Hakim, A.; Fki, M.; Rebaï, T. May antioxidants status depletion by Tetradifon induce secondary genotoxicity in female Wistar rats via oxidative stress? *Pestic. Biochem. Physiol.* **2007**, *88*, 149–155. [[CrossRef](#)]
53. Gohlke, H.; Klebe, G. Approaches to the description and prediction of the binding affinity of small-molecule ligands to macromolecular receptors. *Angew. Chem. Int. Ed.* **2002**, *41*, 2644–2676. [[CrossRef](#)]
54. Soussi, A.; Gargouri, M.; Magné, C.; Ben-Nasr, H.; Kausar, M.A.; Siddiqui, A.; Saeed, M.; Snoussi, M.; Adnan, M.; El-Feki, A.; et al. (–)-Epigallocatechin gallate (EGCG) pharmacokinetics and molecular interactions towards amelioration of hyperglycemia, hyperlipidemia associated hepatorenal oxidative injury in rats. *Chem. Biol. Interact.* **2022**, *368*, 110230. [[CrossRef](#)] [[PubMed](#)]
55. Akacha, A.; Badraoui, R.; Rebai, T.; Zourgui, L. Effect of *Opuntia ficus indica* extract on methotrexate-induced testicular injury: A biochemical, docking and histological study. *J. Biomol. Struct. Dyn.* **2022**, *40*, 4341–4351. [[CrossRef](#)] [[PubMed](#)]

Disclaimer/Publisher's Note: The statements, opinions and data contained in all publications are solely those of the individual author(s) and contributor(s) and not of MDPI and/or the editor(s). MDPI and/or the editor(s) disclaim responsibility for any injury to people or property resulting from any ideas, methods, instructions or products referred to in the content.